Uncertainties in the calibration process of blade tip timing data against finite element model predictions

DOI:
10.1201/9781003132639

Document Version
Accepted author manuscript

Uncertainties in the calibration process of blade tip timing data against finite element model predictions

M E Mohamed[a,b], P Bonello[a], P Russhard[c]
[a]Dept. of Mechanical Aerospace and Civil Engineering, University of Manchester,UK
[b]Faculty of Engineering, Cairo University, Cairo, Egypt
[c]EMTD Ltd, UK

ABSTRACT

Blade stresses are determined from blade tip timing (BTT) data by relating the measured tip deflection to the stresses via Finite Element (FE) models. This process includes some uncertainties due to the following: 1) the shift in the equilibrium position of the blade tip due to steady deflection and/or movements, 2) the change in effective stiffness due to rotation-induced inertia, which affects the BTT-stress calibration factors, 3) the assumption of constant speed over a single revolution that is made in most of BTT algorithms, which is not appropriate for rapid speed rates. This study shows the effect of such uncertainties on the vibration measurement and blade stress estimations.

1. INTRODUCTION

The determination of frequency and amplitude of vibration of turbomachinery blades using BTT algorithms constitutes an essential step towards a full understanding of the dynamic behaviour. The ultimate step involves the estimation of the stress levels corresponding to such measured vibration data, in order to define the fatigue limits of the blades. This latter step requires a validated FE model [1] since BTT vibration data is limited to the blade tip deflection. Unfortunately, the link between FE and BTT is not as yet established or standardised due to complications arising from a number of uncertainties in BTT measurement and data processing on the one hand, and FE modelling on the other. The required calibration factor (i.e. stress-to-displacement ratio in MPa/mm) is determined from FE model predictions of tip nodes displacements and blade stress distribution, and is then applied to the measured BTT displacement to compute the corresponding stress [1]. The predicted tip displacement used in the determination of the calibration factor has to be determined at the node that is nearest to the measurement position, while the predicted stress value can be at any desired location on the blade surface (typically the location of the maximum stress).

Table 1 – BTT Uncertainties

BTT Uncertainties		FEM Uncertainties
-Measurement position, due to: • blade steady movement • probe/blade offset -Coherence (least squares error) -Signal to noise ratio -Number of probes	-Condition number -Filtering -Zeroing -Averaging -Time resolution	-Measurement position -Model validation tolerances -Non-homogenous material properties -Mistuning

The uncertainties associated with BTT measurements and analysis, in addition to those of FE modelling, have to be considered in order to achieve the best results. If all uncertainties are controlled, the current BTT capability could produce end-to-end stress measurements with uncertainty of only +/- 2.5% or better [2]. The sources of uncertainty associated with both BTT and FEM are listed in Table 1 based on previous studies [1–5]. Jousselin et al. [6] presented a method for establishing the levels of uncertainty for the blade tip displacement amplitudes measured by a BTT system. Russhard [2] studied the levels of most of the aforementioned uncertainties and showed that mostly depend on the operator, who must be highly experienced to avoid extreme uncertainty levels [2].

Uncertainty in the mean position of the probe (the sensing position) relative to the blade tip affects both the BTT measurements and the calibration of the data against FE predictions. It arises from two sources [7]: (a) positional errors (offsets) during installation of the probes and/or blades; (b) steady (non-oscillatory) deviations of the blade tip from its mean position and orientation, which are caused by the changes in the speed dependant operating conditions, such as thermal expansion and axial float of the rotor, bearing wear, and non-uniform gas loading [7]. The measurement position uncertainty considered in this paper is of type (b) since it is more problematic due to the variation of the associated positional error with speed (in contrast to (a), where the positional error is independent of speed) [7]. This shift (of the probe measurement point from its nominal position relative to the blade tip) can have a great impact on the calibration factor relating tip deflection to stress, since both the original and new points may have different amplitudes of vibration, thus introducing errors into the stress and the fatigue limit estimates.

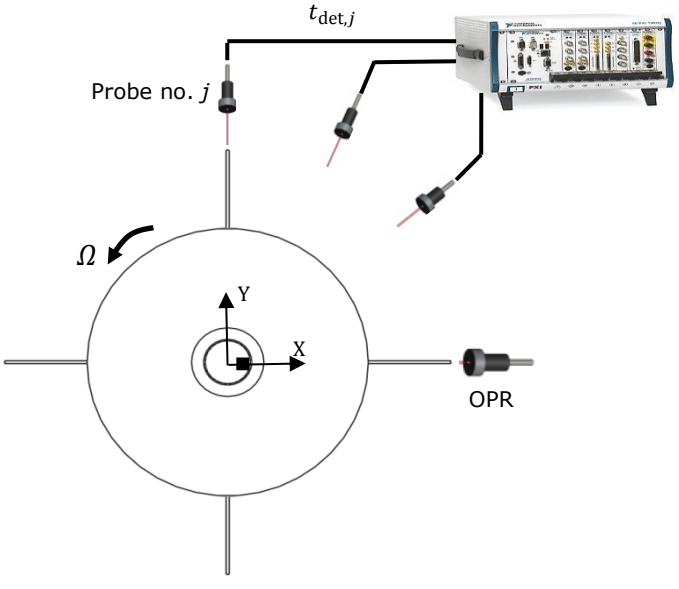

Figure 1 – BTT Measurement System

Turbomachinery blades are typically modelled using rotating cantilever beam models, which have vibration characteristics that vary significantly with speed changes [8]. One of the factors responsible for this variation is the centrifugal inertia force, which causes a significant stretch in the blades, resulting in a change in their effective bending stiffness. Some studies have considered centrifugal

stiffening, and other rotation-induced inertia effects in shaft-blisk (i.e. bladed disk) assemblies, and showed their effects on the natural frequencies of the rotating systems [9,10]. However, stress stiffening does not only change the natural frequencies, but also affects the calibration factors, as will be shown in this work.

Traditional methods of BTT data processing assume that the rotational speed is constant over the course of a single revolution [11]. In reality, it is impossible for the rotational speed to keep constant [12]. Moreover, this assumption is incorrect in the case of transient rotor speeds [11] especially when the rate of change of speed ("speed rate" in rpm/rev) is high. Especially in the latter case, it is therefore expected that the constant speed assumption will result in noticeable errors in the estimated stress values as well as the vibration levels. Currently, some research studies are concerned with the development of measurement systems for applications involving significant speed rate [11–15].

This study shows for the first time the effects of three sources of uncertainty on the BTT vibration measurement and blade stress estimations: 1) Probe measurement position, 2) Centrifugal stiffening, and 3) High-rate speed change. A BTT simulator that has been presented by the authors in [16,17] is used to generate the simulated BTT data including the considered effects under controlled conditions. A new approach for the calculations of both strain and stress values simultaneously with the BTT displacement data using the simulator is presented.

2. BLADE TIP TIMING

BTT systems involve the use of a number of circumferentially distributed non-contact probes j, $j = 1, \ldots., N_{\mathrm{Pr}}$ and a data acquisition system as shown in Figure 1 to detect and acquire the arrival times $t_{\mathrm{det},j}$ of all blades at the probe angular locations during every revolution [16]. The arrival time is the time at which a blade tip passes within the range of a probe. Another probe, known as the once per revolution (OPR) probe, is typically used to detect the start/end time of every revolution, from which the following information can be calculated: (1) the average rotational speed over the revolution; (2) the number of completed revolutions; (3) the expected times of arrival $t_{\mathrm{exp},j}$ of the blades past the probes if the assembly rotates as a rigid body. It is noted that some researchers have proposed to generate such information from the blade arrival times without need of the OPR [18,19]. The collected BTT data are then processed in order to determine the blade tip displacements as follows

$$d_j = \Omega R \Delta t_j \tag{1}$$

where d_j is the tip displacement in the plane of rotation ($X-Y$ plane) at probe no. j, Ω is the average angular speed (rad/s) over a single revolution [20], R is the radius of the blade tip measured from the centre of rotation, and Δt_j is the difference between the blade's expected and detected arrival times.

$$\Delta t_j = t_{\mathrm{exp},j} - t_{\mathrm{det},j} \tag{2}$$

The BTT displacement data are analysed in order to determine the vibration parameters (amplitude, frequency, and phase), and the equivalent stress levels are then calculated using FE-based calibration factors.

3. PROBE MEASUREMENT POSITION ERROR

Probe measurement position errors have significant effect on the estimation

of stress levels in blades from BTT measurements. The errors considered are those arising from the blade steady movement, which can be resolved into three components (rotor axial shift, blade lean, and blade untwist). Figure 2 shows a blade tip that shifts axially (parallel to the axis of rotation Z). Initially (with no steady movement), the optical probe's laser beam intersects with the blade tip at point (1) which has the same axial position of the probe. Once their angular positions agree, the time is recorded as $t_{\mathrm{det},j})_1$, and the displacement is calculated from Eq (1) using the value of $t_{\mathrm{exp},j})_1$, where the difference between both times $(\Delta t_j)_1$ is proportional to the instantaneous displacement at point (1). If the blade moves axially by an amount $\Delta u^{(\mathrm{off})}$, the measurement position will shifted to point (2) and the recorded arrival time is denoted as $t_{\mathrm{det},j})_2$. The expected arrival time for point (2) will be different from point (1) but, since the movement is unknown, the instantaneous displacement at (2) is calculated using $\Delta t_j)_2 = t_{\mathrm{exp},j})_1 - t_{\mathrm{det},j})_2$ in Eq (1). There are therefore two errors: 1) a "DC" error due to the use of $t_{\mathrm{exp},j})_1$; 2) the vibration is being measured at point (2) rather than point (1) and the vibration amplitudes at these points are typically different. The DC error can be removed by the method presented in [7], while the second error will result in wrong stress estimation unless the calibration factor is updated to refer to point (2). The method of [7] makes this possible since it allows the quantification of the steady movement and thus the location of the new sensing point (2) on the blade tip.

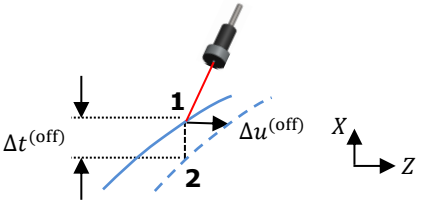

Figure 2 – Probe Measurement Position Error

4. CENTRIFUGAL STIFFENING

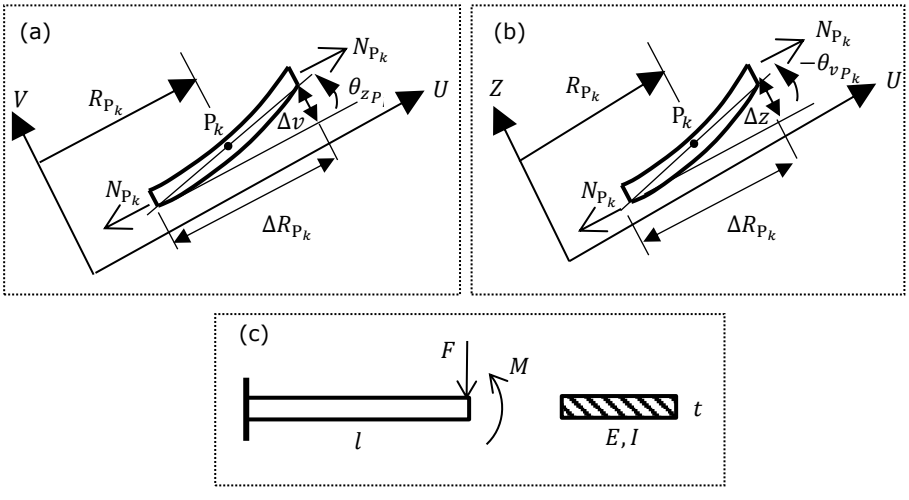

Figure 3 – Centrifugal Stiffening, a) Blisk Segment (*UV*-plane), b) Blisk

Segment (*UZ*-plane), c) fixed-free beam with force and moment loading

The centrifugal inertia tension N_{P_k} on a blisk segment with mass centre P_k $(R_{\mathrm{P}_k}, \vartheta_{\mathrm{P}_k}, Z_{\mathrm{P}_k})$ and radial extent ΔR_{P_k} can be calculated as [17]:

$$N_{\mathrm{P}_k} = \Omega^2 \{\textstyle\sum_{j=1}^{J} \Delta m_j R_j\}\big|_{R_1 = R_{P_k}} \tag{3}$$

where the summation is applied to radial segments with mass centres located along the same angular and axial position of P_k $(\vartheta_{\mathrm{P}_k}, Z_{\mathrm{P}_k})$ and proceeding radially outward. With reference to Figure 3(a,b), the centrifugal tension N_{P_k} stiffens the segment by inducing moments in the edge-wise (*UV*) and flap-wise (*UZ*) planes ($M_{z_{\mathrm{P}_k}}$, $M_{v_{\mathrm{P}_k}}$ respectively) which oppose the corresponding angular deformations $\theta_{z_{\mathrm{P}_k}}$, $\theta_{v_{\mathrm{P}_k}}$:

$$\begin{aligned} M_{z_{\mathrm{P}_k}} &= -N_{\mathrm{P}_k}\Delta v = -N_{\mathrm{P}_k}\Delta R_{\mathrm{P}_k}\tfrac{\Delta v}{\Delta R_{\mathrm{P}_k}} = -N_{\mathrm{P}_k}\Delta R_{\mathrm{P}_k}\theta_{z_{\mathrm{P}_k}} \\ M_{v_{\mathrm{P}_k}} &= N_{\mathrm{P}_k}\Delta z = N_{\mathrm{P}_k}\Delta R_{\mathrm{P}_k}\tfrac{\Delta z}{\Delta R_{\mathrm{P}_k}} = -N_{\mathrm{P}_k}\Delta R_{\mathrm{P}_k}\theta_{v_{\mathrm{P}_k}} \end{aligned} \tag{4}$$

where Δv, and Δz are the deflections in V and Z directions respectively. In order to understand the effect of the above moments on the calibration factors and estimated values of stresses from BTT measurements, the simple cantilever shown in Figure 3(c) is considered. The cantilever is subjected to a force (F) at the free end. The maximum deflection and maximum stress of the segment can be respectively calculated as

$$d_{\max)_F} = \tfrac{FL^3}{3EI} \quad , \quad \sigma_{\max)_F} = \tfrac{FL(t/2)}{I} \tag{5}$$

The calibration factor C can then be determined as

$$C_1 = \tfrac{\sigma_{max)F}}{d_{max)F}} = \tfrac{3E(t/2)}{L^2} \tag{6}$$

Now, considering a moment M applied at the free end of the segment, in addition to F, the maximum deflection and stress due to the total effect become

$$d_{\max)_{\mathrm{tot}}} = \tfrac{FL^3}{3EI} - \tfrac{ML^2}{2EI} \quad , \quad \sigma_{\max)_{\mathrm{tot}}} = \tfrac{FL(t/2)}{I} - \tfrac{M(t/2)}{I} \tag{7}$$

The new calibration factor will be

$$C_2 = \tfrac{\sigma_{\max)_{\mathrm{tot}}}}{d_{\max)_{\mathrm{tot}}}} = \tfrac{\left(\frac{FL(t/2)}{I} - \frac{M(t/2)}{I}\right)}{\left(\frac{FL^3}{3EI} - \frac{ML^2}{2EI}\right)} = \tfrac{(FL-M)}{\left(FL - \frac{3}{2}M\right)} \times \tfrac{3E(t/2)}{L^2} \tag{8}$$

Substituting from Eq (6) into Eq (8)

$$C_2 = \tfrac{(FL-M)}{\left(FL - \frac{3}{2}M\right)} \times C_1 \tag{9}$$

From Eq (9) it should be clear that, for the actual blade whose generic segment is shown in Figure 3(a,b), the moments induced by the centrifugal effect will affect the calibration factor (reference location stress to tip deflection).

5. HIGH SPEED RATES

BTT processing algorithms assume that the rotational speed is constant over a single revolution [20], which is not valid in case of time-varying speed. In such a

case, assuming linear variation in speed from Ω_{i} rad/s to Ω_{f} rad/s over a duration T_{s}, the rotational speed at any time t can be calculated using the following formula:

$$\Omega(t) = \Omega_{\mathrm{i}} + \left(\frac{\Omega_{\mathrm{f}} - \Omega_{\mathrm{i}}}{T_{\mathrm{s}}}\right) t \tag{10}$$

Therefore, the BTT displacement at each probe should be calculated from Eq (1) using different values of speed based on Eq (10). The general form of the blade tip displacement d_j measured at probe no. j after processing (minimization of noise and offset) is assumed to follow the following form [16]

$$d_j = a_0 + \sum_{m=1}^{M} \left(a_{1m} \sin\left(\mathrm{EO}_m \Omega t_j\right) + a_{2m} \cos\left(\mathrm{EO}_m \Omega t_j\right)\right) \tag{11}$$

where EO_m is the engine order of excitation no. m, $m = 1,2,..,M$, whose frequency $\omega_m = \mathrm{EO}_m \Omega$, and t_j is the sampling time at probe no. j during revolution no. n according to the above assumed fit. For a constant rotational speed Ω, $t_j = t_{j,n=1} + (n-1)\, 2\pi/\Omega$, $n = 1,2,\ldots$ and so, the term $\mathrm{EO}_m \Omega t_j = \mathrm{EO}_m \Omega \{t_{j,n=1} + (n-1)\, 2\pi/\Omega\}$ always represents the same angle $\mathrm{EO}_m \Omega t_{j,n=1}$ provided EO_m is a fixed integer. Hence, Eq. (11) can then be rewritten in terms of the fixed probe angular position $\theta_j = \Omega t_{j,n=1}$:

$$d_j = a_0 + \sum_{m=1}^{M} \left(a_{1m} \sin\left(\mathrm{EO}_m \theta_j\right) + a_{2m} \cos\left(\mathrm{EO}_m \theta_j\right)\right) \tag{12}$$

The representation of Eq. (12) is used in some of the main BTT analysis algorithms, such as the two parameter plot [21] and sine fitting with data preparation methods [22]. As shown above, it is only valid if the rotational speed Ω is either constant or assumed to be approximately constant over one revolution, while varying gradually over time. Therefore, this assumption is not valid in case of high speed rates (rpm/rev), and may therefore result in large amount of errors in the estimated stress values. The speed rate can be calculated as

$$\text{Speed rate (rpm/rev)} = \frac{60(\Omega_{\mathrm{f}} - \Omega_{\mathrm{i}})}{\left(\frac{\Omega_{\mathrm{f}} + \Omega_{\mathrm{i}}}{2}\right) T_{\mathrm{s}}} \tag{13}$$

6. BTT SIMULATION

The following sections include descriptions of the FE model, and the BTT simulator used to generate simulated BTT displacements and blade stresses, in order to examine the effects of the abovementioned sources of uncertainty on the stress estimates.

6.1 FE model

The shaft-blisk system shown in Figure 1 was analysed before in [17,23] to study the effect of rotation-induced inertia on the natural frequencies of the rotating assembly. The system consists of a stepped circular cross-section shaft supported by two bearings (with equal stiffness in the two orthogonal directions 1.5×10^7 N/m) and carrying a disk with four blades, the material is the same for all components (density 7800 kg/m^3, Young Modulus 200 GPa). The FE model has been created using *ANSYS*, and the total number of degrees of freedom is 1800858. Both ends of the shaft were assumed to be constrained from axial motion and the left hand end constrained from torsional motion. Modal analysis has been carried out, and some of the resulting zero-speed natural frequencies and their corresponding mode shapes are shown in Table 2 and Figure 4 respectively.

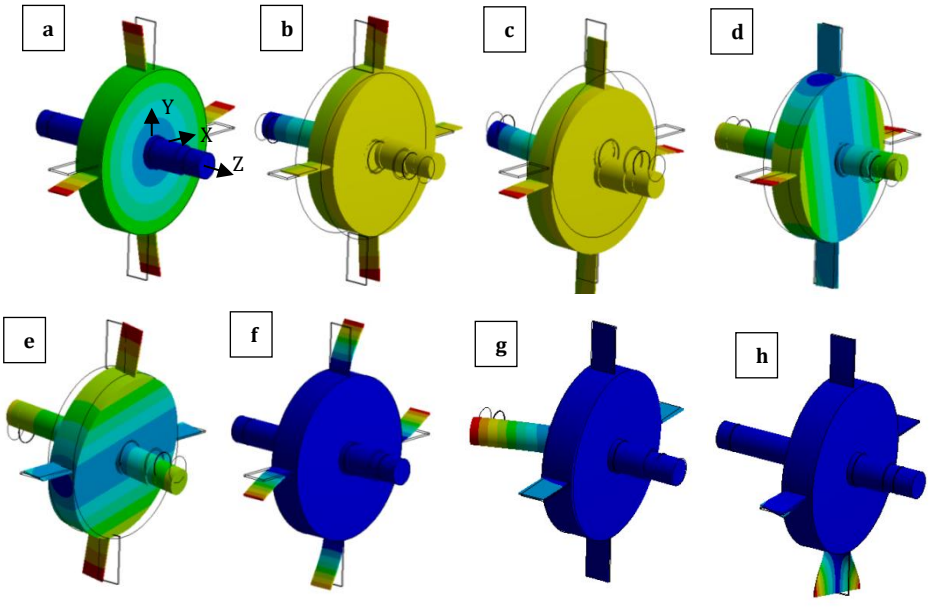

Figure 4 – Mode shapes: a) mode 1, b) mode 2, c) mode 3, d) mode 4, e) mode 5, f) mode 6, g) mode 10, h) mode 15.

Table 2 – Natural Frequencies of the shaft-Blisk Assembly

Mode	1	2	3	4	5	6	10	15
Natural frequency (Hz)	121.7	133.8	133.8	266.5	266.5	364.3	1156.5	1464

6.2 BTT simulator

A simulator that is based on a realistic (FE-derived) multi-modal model of the blisk was presented by the authors in [16], and upgraded for the inclusion of rotation-induced inertia effects in [17]. The following section includes a brief description of the simulator.

If $\mathbf{u}(t)$ denotes the $3K \times 1$ vector containing the instantaneous absolute coordinates of the nodes P_k $(k = 1 \ldots K)$ on the tip of a given blade, the simulator computes $\mathbf{u}(t)$ by adding the three components that contribute to it: (A) the absolute coordinates after rigid body rotation from a reference angular position; (B) the steady shift; (C) the dynamic response. The last component is determined by calculating the dynamic excitation response $\mathbf{\Delta u}^{(\mathrm{def})}(t)$ of the non-rotating blisk in the reference angular position and then transforming it according to the rigid rotation angle prior to addition to (A) and (B). $\mathbf{\Delta u}^{(\mathrm{def})}(t)$ is calculated from a transformation to modal space using as basis functions the first *H* natural undamped modes of vibration of the non-rotating blisk in the reference angular position:

$$\mathbf{\Delta u}^{(\mathrm{def})}(t) = \mathbf{H}_{\mathrm{P}}\mathbf{q}(t) \tag{14}$$

where the $H \times 1$ vector of modal co-ordinates $\mathbf{q}(t)$ is governed by the modal equations of motion:

$$\ddot{\mathbf{q}}(t) + \mathrm{diag}([\cdots 2\zeta_r\varpi_r \cdots])\dot{\mathbf{q}}(t) + \mathrm{diag}([\cdots \varpi_r^2 \cdots])\mathbf{q}(t) = \mathbf{H}_\mathbf{f}^\mathrm{T}\mathbf{f}(t) \quad (15)$$

$\mathbf{H}_\mathrm{P}$, $\mathbf{H}_\mathbf{f}$ are modal transformation matrices whose H columns are mass-normalised eigenvectors corresponding to the natural circular frequencies ϖ_r $(r = 1, \dots, H)$, ζ_r is the modal damping ratio, added to ensure decay of transients. $\mathbf{f}(t)$ is the vector of dynamic excitation forces applied to the blisk. In the above approach, the blisk is divided into radial/angular segments and the rotational inertia effects from the individual segments, with mass centres at selected FE nodes P_k $(k = 1 \dots K)$, are summed over the entire system and added as additional "external" forces to the modal equation (Eq (15)).

The simulator is implemented in *Matlab*/*Simulink* and solves Eq. (15) using a numerical integration routine with automatic time-step control. At each time step it determines $\mathbf{u}(t)$ by combining its three components. For a given configuration of probes, $t_{\mathrm{exp},j}$ is determined by locating the passing time of the node on the blade tip that coincides with the angular and axial position of probe no. j using only the rigid rotation component of $\mathbf{u}(t)$. The actual arrival time $t_{\mathrm{det},j}$ is determined in the same way but using $\mathbf{u}(t)$. The blade tip displacements d_j are then determined as per Eqs. (1) and (2) and corrupted with Gaussian white noise of prescribed noise-to-signal ratio (NSR) to simulate AC measurement noise.

6.3 Determination of strain and stress values using the simulator

Figure 5(a) shows the stress map on a blade surface using FEM and indicates the position of maximum stress. This is usually the way the positions of the strain gauges (SGs) on the blade surface are selected. A strain rosette (a set of three SGs a, b, and c) is placed and glued to the surface at the desired location as shown in Figure 5(b) with a known orientation of each SG with respect to a specified reference. It can be assumed that the surface area including the strain rosette is flat due to the small sizes of the SGs, and thus the rosette is assumed to be in one plane $x'y'$. In the case of the simulator, the strain values can be obtained in a similar way to that used with physical SGs as follows.

-An FE node o is selected at the desired position on the blade surface.
-Three other nodes $\mathrm{a}, \mathrm{b}, \mathrm{c}$ are selected as close as possible to the node o as shown in Figure 5(c), so they can be considered in one plane $x'y'$ where x' and y' are orthogonal axes intersecting at the node o.
-$\mathrm{oa}, \mathrm{ob}, \mathrm{and}\ \mathrm{oc}$ represent the strain rosette, and the distances $\overline{\mathrm{oa}}, \overline{\mathrm{ob}}, \mathrm{and}\ \overline{\mathrm{oc}}$ can be calculated using the coordinates of the nodes before deformation with respect to the rotating local reference frame xyz as

$$\begin{aligned}
\overline{\mathrm{oa}} &= \sqrt{(x_\mathrm{a} - x_\mathrm{o})^2 + (y_\mathrm{a} - y_\mathrm{o})^2 + (z_\mathrm{a} - z_\mathrm{o})^2} \\
\overline{\mathrm{ob}} &= \sqrt{(x_\mathrm{b} - x_\mathrm{o})^2 + (y_\mathrm{b} - y_\mathrm{o})^2 + (z_\mathrm{b} - z_\mathrm{o})^2} \\
\overline{\mathrm{oc}} &= \sqrt{(x_\mathrm{c} - x_\mathrm{o})^2 + (y_\mathrm{c} - y_\mathrm{o})^2 + (z_\mathrm{c} - z_\mathrm{o})^2}
\end{aligned} \quad (16)$$

The angles $\theta_\mathrm{a}, \theta_\mathrm{b}, \theta_\mathrm{c}$ are calculated by assuming that x' coincides with the vector $\overrightarrow{\mathrm{oa}}$, so $\theta_\mathrm{a} = 0$, and then the angles $\theta_\mathrm{b}, \mathrm{and}\ \theta_\mathrm{c}$ of the vectors $\overrightarrow{\mathrm{ob}}$ and $\overrightarrow{\mathrm{oc}}$ respectively are obtained, knowing that all the vectors are assumed to be in the same plane:

$$\cos\theta_b = \frac{\overrightarrow{\mathrm{ob}} \cdot \overrightarrow{\mathrm{oa}}}{|\overrightarrow{\mathrm{ob}}| \cdot |\overrightarrow{\mathrm{oa}}|} \quad (17)$$

where $$\overrightarrow{\mathrm{ob}} \cdot \overrightarrow{\mathrm{oa}} = (x_\mathrm{b} - x_\mathrm{o})(x_\mathrm{a} - x_\mathrm{o}) + (y_\mathrm{b} - y_\mathrm{o})(y_\mathrm{a} - y_\mathrm{o}) + (z_\mathrm{b} - z_\mathrm{o})(z_\mathrm{a} - z_\mathrm{o}) \quad (18)$$

-The same distances are calculated again at a time t including deformation:

$$\begin{aligned}\overline{\mathrm{oa}}(t) &= \sqrt{(x_\mathrm{a}(t)-x_\mathrm{o}(t))^2+(y_\mathrm{a}(t)-y_\mathrm{o}(t))^2+(z_\mathrm{a}(t)-z_\mathrm{o}(t))^2}\\ \overline{\mathrm{ob}}(t) &= \sqrt{(x_\mathrm{b}(t)-x_\mathrm{o}(t))^2+(y_\mathrm{b}(t)-y_\mathrm{o}(t))^2+(z_\mathrm{b}(t)-z_\mathrm{o}(t))^2}\\ \overline{\mathrm{oc}}(t) &= \sqrt{(x_\mathrm{c}(t)-x_\mathrm{o}(t))^2+(y_\mathrm{c}(t)-y_\mathrm{o}(t))^2+(z_\mathrm{c}(t)-z_\mathrm{o}(t))^2}\end{aligned} \tag{19}$$

where $x(t) = x + \Delta x(t)$, $y(t) = y + \Delta y(t)$, $z(t) = z + \Delta z(t)$, and $\Delta x(t)$, $\Delta y(t)$, $\Delta z(t)$ are the elements of $\Delta\mathbf{u}^{(\mathrm{def})}(t)$ corresponding to the nodes $\mathrm{o}, \mathrm{a}, \mathrm{b}, \mathrm{c}$.

Finally, the strain values can be calculated as

$$\varepsilon_{\mathrm{oa}}(t) = \frac{\overline{\mathrm{oa}}(t)-\overline{\mathrm{oa}}}{\overline{\mathrm{oa}}}\ ,\ \varepsilon_{\mathrm{ob}}(t) = \frac{\overline{\mathrm{ob}}(t)-\overline{\mathrm{ob}}}{\overline{\mathrm{ob}}}\ ,\ \varepsilon_{\mathrm{oc}}(t) = \frac{\overline{\mathrm{oc}}(t)-\overline{\mathrm{oc}}}{\overline{\mathrm{oc}}} \tag{20}$$

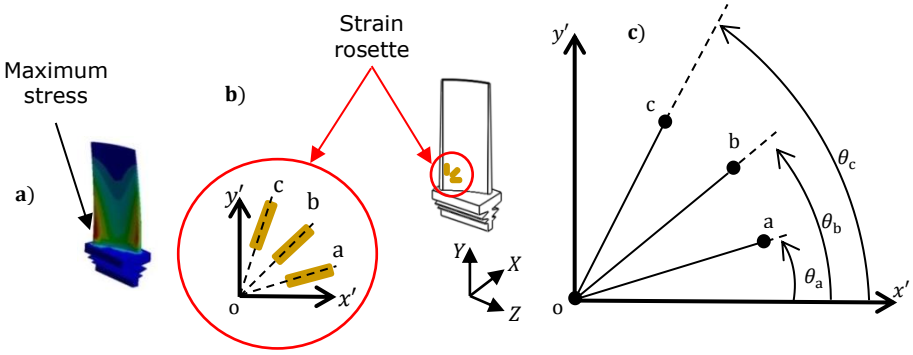

Figure 5 – a) Blade stress map, b) SG rosette, c) Strain vectors.

Now, for the calculations of the stresses, the strain values are transformed into the orthogonal directions x' and y' using the following equations

$$\begin{aligned}\varepsilon_{\mathrm{oa}} &= \varepsilon_{x'}\cos^2\theta_\mathrm{a} + \varepsilon_{y'}\sin^2\theta_\mathrm{a} + \gamma_{x'y'}\sin\theta_\mathrm{a}\cos\theta_\mathrm{a}\\ \varepsilon_{\mathrm{ob}} &= \varepsilon_{x'}\cos^2\theta_\mathrm{b} + \varepsilon_{y'}\sin^2\theta_\mathrm{b} + \gamma_{x'y'}\sin\theta_\mathrm{b}\cos\theta_\mathrm{b}\\ \varepsilon_{\mathrm{oc}} &= \varepsilon_{x'}\cos^2\theta_\mathrm{c} + \varepsilon_{y'}\sin^2\theta_\mathrm{c} + \gamma_{x'y'}\sin\theta_\mathrm{c}\cos\theta_\mathrm{c}\end{aligned} \tag{21}$$

which can be formulated in a matrix form as

$$\begin{bmatrix}\cos^2\theta_\mathrm{a} & \sin^2\theta_\mathrm{a} & \sin\theta_\mathrm{a}\cos\theta_\mathrm{a}\\ \cos^2\theta_\mathrm{b} & \sin^2\theta_\mathrm{b} & \sin\theta_\mathrm{b}\cos\theta_\mathrm{b}\\ \cos^2\theta_\mathrm{c} & \sin^2\theta_\mathrm{c} & \sin\theta_\mathrm{c}\cos\theta_\mathrm{c}\end{bmatrix}\begin{bmatrix}\varepsilon_{x'}\\ \varepsilon_{y'}\\ \gamma_{x'y'}\end{bmatrix} = \begin{bmatrix}\varepsilon_{\mathrm{oa}}\\ \varepsilon_{\mathrm{ob}}\\ \varepsilon_{\mathrm{oc}}\end{bmatrix} \tag{22}$$

or, $\mathbf{Ba} = \mathbf{c}$

By solving the above equation as $\mathbf{a} = \mathbf{B}^{-1}\mathbf{c}$, The values of normal and shear strain in $x'y'$ plane are obtained. Assuming plane stress conditions, and by using the stress-strain relations

$$\varepsilon_{x'} = \frac{1}{E}\left[\sigma_{x'} - \nu\sigma_{y'}\right]\ ,\ \varepsilon_{y'} = \frac{1}{E}\left[\sigma_{y'} - \nu\sigma_{x'}\right]\ ,\ \gamma_{x'y'} = \frac{\tau_{x'y'}}{G} \tag{23}$$

The stress values can be determined, and then the principal plane stresses and maximum in-plane shear stress are calculated as

$$\begin{aligned}\sigma_{1,2} &= \frac{\sigma_{x'}+\sigma_{y'}}{2} \pm \sqrt{\left(\frac{\sigma_{x'}-\sigma_{y'}}{2}\right)^2 + {\tau_{x'y'}}^2}\\ \tau_{\max} &= \sqrt{\left(\frac{\sigma_x-\sigma_x}{2}\right)^2 + {\tau_{xy}}^2}\end{aligned} \tag{24a,b}$$

Finally, the equivalent (Von Mises) stress is calculated as

$$\sigma_e = \frac{1}{\sqrt{2}}[(\sigma_1 - \sigma_2)^2 + (\sigma_2 - \sigma_3)^2 + (\sigma_3 - \sigma_1)^2]^{1/2} \quad (25)$$

where $\sigma_3 = 0$.

7. RESULTS AND DISCUSSIONS

7.1 Effect of probe measurement position error

Considering the torsional mode shape of blade shown in Figure 4(h), the amplitude of deformation at the blade tip is seen to vary significantly, being maximum at both ends and tending to zero at the midpoint. Assuming that a probe is located at one of the ends (initial measurement point), and calculating the modal displacements at all tip locations relative to the initial measurement point, the percentage error in BTT displacement due to the shift of the blade along the axial direction (axis of rotation *Z*) is as shown in Figure 6. The data in Figure 6 were computed using the formula in Eq (26), where d_{end} is the displacement at the tip's end (initial sensing location), and d_z is the displacement along *Z*-axis at any other location on the tip.

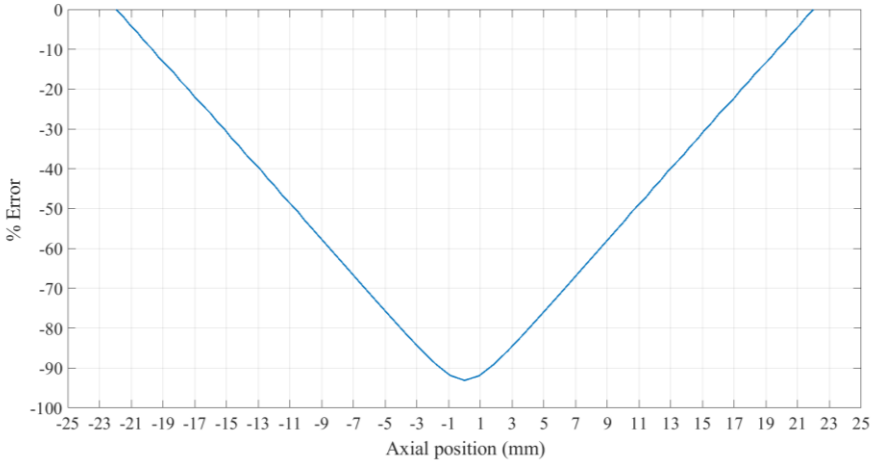

Figure 6 – Percentage error of tip displacement along the axial direction relative to the displacement at the tip end.

$$\%\ \text{error} = \frac{d_z - d_{\text{end}}}{d_{\text{end}}} \times 100 \quad (26)$$

Table 3 – Effect of stagger angle on probe measurement position error

Stagger angle (degrees)	0	10	20	30	40	45
% error/mm	4.37	4.42	4.64	5.03	5.69	6.16

It is clear from Figure 6 that the error in displacement value would be about 4.37% per 1 mm shift in measurement position. The rate of error was also examined at different stagger angles of blade (angle between the blade's chord and the line parallel to the axis of rotation i.e. *Z*-axis) and the results listed in Table 3 show that the error increases to a value of 6.16%/mm at an angle of $45°$. Moreover, complex blade profiles in which the blade tip nodes have different distances from the blade root can result in similar errors in the case of blade bending modes, due to the

different displacement values at the tips. These errors will then be propagated to the estimated stress values.

7.2 Effect of centrifugal stiffening

For preliminary checking, the stress/tip displacement calibration factor in the absence of centrifugal stiffening was first determined by performing harmonic analysis in *ANSYS*. A harmonic force was applied at the tip of one of the blades in the *x*-direction with a frequency equal to the 1st natural frequency (i.e. 121.7 Hz, see Table 2). The displacement at the tip, and the corresponding maximum stress values, were then extracted and the calibration factor calculated as 136.7 MPa/mm.

In order to study the effect of centrifugal stiffening on the calibration factor as discussed in section 4, the BTT simulator (section 6.2) was then used to generate the dynamic response values at the desired FE nodes of both the blade surface and tip, and the stress value was then calculated at the position of maximum stress using the method described in section 6.3. The simulation was implemented using the same harmonic force excitation as the above described *ANSYS* study. In the absence of centrifugal inertia effects, the resulting calibration factor was 131.24 MPa/mm, which is only 4 % less than the one determined by *ANSYS.* The simulation was then repeated by considering the centrifugal stiffening of the blisk. The Campbell diagram generated first in order to determine the new value of the critical speed with respect to the first mode, and it is found to be 434.6 rev/s (i.e. up from 121.7 rev/s at no rotation). The excitation frequency was then updated, and the responses were extracted and processed to calculate the new calibration factor, which was found to be 142.6 MPa/mm i.e. 8.6 % higher than the initial one. This agrees with the explanation presented in section 4.

7.3 Effect of high speed rate

It has been explained in section 5 that the significant variation in speed over one revolution results in an error in the calculated values of vibration amplitude, due to inaccurate displacement values at the probes (unless Eq (10) is used in Eq (1)), and, more significantly, the invalid assumption of the BTT displacement form (Eq (12)). A number of simulations were done with the same excitation conditions and the same range of speeds (0 to 250 rev/s) that includes the first critical speed (Engine Order (EO)=1), but with different speed rates. The generated BTT displacements were analysed using the multi-frequency sine fitting with data preparation method [22], and the resulting amplitude of vibration was compared to the zero-to-peak value of vibration response time history, giving the error values listed in Table 4.

Table 4 – BTT displacement error vs speed rate

Speed rate rpm/rev	24	120	1200	2400
% error	1.6	4.2	25	42

These results clearly show the significant adverse effect of high speed rate on the accuracy of the estimated values of tip displacement. Such errors would then of course be propagated to the estimated blade stresses.

8. CONCLUSIONS

The determination of blade vibration using BTT, and the estimation of the corresponding stresses, are subject to a number of uncertainties related to both measurement and FE modelling. Three sources of uncertainty were analysed with the aim of quantifying their effects, which were then illustrated for three specific cases. Probe measurement position error resulted in an error in tip displacement of

about 4% per mm shift of the blade, and this error increased with the stagger angle of the blade. Centrifugal stiffening resulted in an increase of 8.6% in the stress/tip deflection calibration factor. A high speed rate of 2400 rpm/rev may result in more than 40% error in vibration amplitude. Unless such sources of uncertainty are considered in the end-to-end process for the estimation of stress levels from BTT data, their combined effect may result in a large margin of error.

ACKNOWLEDGMENT

This work is part of the EU research project Batista (Blade Tip Timing System Validator) - Clean Sky 2 - 862034, funded by the EU Commission (H2020 CS2).

REFERENCES

[1] Russhard, P., 2010, "Development of a Blade Tip Timing Based Engine Health Monitoring System," Ph.D. dissertation, University of Manchester, Manchester, United Kingdom.

[2] Russhard, P., 2016, "Blade Tip Timing (BTT) Uncertainties," AIP Conference Proceedings, 1740.

[3] Jousselin, O., 2013, "Development of Blade Tip Timing Techniques in Turbo Machinery," Ph.D. dissertation, The University of Manchester, Manchester, United Kingdom.

[4] Lawson, C., and Ivey, P., 2003, "Compressor Blade Tip Timing Using Capacitance Tip Clearance Probes," Proceedings of ASME Turbo Expo 2003, Atlanta, Georgia, USA, pp. 1–8.

[5] Knappett, D., and Garcia, J., 2008, "Blade Tip Timing and Strain Gauge Correlation on Compressor Blades," Proceedings of the Institution of Mechanical Engineers, Part G: Journal of Aerospace Engineering, 222(4), pp. 497–506.

[6] O. Jousselin, P. Russhard, and P. Bonello, 2012, "A Method for Establishing the Uncertainty Levels for Aero-Engine Blade Tip Amplitudes Extracted from Blade Tip Timing Data," Proceedings of the 10th International Conference on Vibrations in Rotating Machinery, pp. 211–220.

[7] Mohamed, M., Bonello, P., and Russhard, P., 2019, "A Novel Method for the Determination of the Change in Blade Tip Timing Probe Sensing Position due to Steady Movements," Mechanical Systems and Signal Processing, 126, pp. 686–710.

[8] Przemieniecki, J. S., 1985, Theory of Matrix Structural Analysis., McGraw-Hill, New York.

[9] Chun, S.-B., and Lee, C.-W., 1996, "Vibration Analysis of Shaft-Bladed Disk System by Using Substructure Synthesis and Assumed Modes Method," Journal of Sound and Vibration, 189(5), pp. 587–608.

[10] Chiu, Y.-J., Li, X.-Y., Chen, Y.-C., Jian, S.-R., Yang, C.-H., and Lin, I.-H., 2017, "Three Methods for Studying Coupled Vibration in a Multi Flexible Disk Rotor System," Journal of Mechanical Science and Technology, 31(11), pp. 5219–5229.

[11] Diamond, D. H., Heyns, P. S., and Oberholster, A. J., 2019, "Improved Blade Tip Timing Measurements during Transient Conditions Using a State Space Model," Mechanical Systems and Signal Processing, 122, pp. 555–579.

[12] Chen, Z., Liu, J., Zhan, C., He, J., and Wang, W., 2018, "Reconstructed Order Analysis-Based Vibration Monitoring under Variable Rotation Speed by Using Multiple Blade Tip-Timing Sensors," Sensors, 18(10), p. 3235.

[13] Fan, C., Wu, Y., Russhard, P., and Wang, A., 2020, "An Improved Blade Tip-Timing Method for Vibration Measurement of Rotating Blades During Transient Operating Conditions," Journal of Vibrational Engineering and Technologies, (0123456789).

[14] Ji-wang, Z., Lai-bin, Z., Ke-Qin, D., and Li-xiang, D., 2018, "Blade Tip-Timing Technology with Multiple Reference Phases for Online Monitoring of High-Speed Blades under Variable-Speed Operation," Measurement Science Review, 18(6), pp. 243–250.
[15] Bouchain, A., Picheral, J., Lahalle, E., Chardon, G., Vercoutter, A., and Talon, A., 2019, "Blade Vibration Study by Spectral Analysis of Tip-Timing Signals with OMP Algorithm," Mechanical Systems and Signal Processing, 130, pp. 108–121.
[16] Mohamed, M. E., Bonello, P., and Russhard, P., 2020, "An Experimentally Validated Modal Model Simulator for the Assessment of Different Blade Tip Timing Algorithms," Mechanical Systems and Signal Processing, 136, p. 106484.
[17] Mohamed, M., 2019, "Towards Reliable and Efficient Calibration of Blade Tip Timing Measurements against Finite Element Predictions," Ph.D. dissertation, University of Manchester.
[18] Gallego-Garrido, J., Dimitriadis, G., Carrington, I., and Wright, J., 2007, "A Class of Methods for the Analysis of Blade Tip Timing Data from Bladed Assemblies Undergoing Simultaneous Resonances—Part II: Experimental Validation," International Journal of Rotating Machinery, pp. 1–10.
[19] Carrington, I., Wright, J., Cooper, J., and Dimitriadis, G., 2001, "A Comparison of Blade Tip Timing Data Analysis Methods," Proceedings of the Institution of Mechanical Engineers, Part G: Journal of Aerospace Engineering, 215(5), pp. 301–312.
[20] Russhard, P., 2014, "Derived Once per Rev Signal Generation for Blade Tip Timing Systems," Instrumentation Symposium 2014, IET & ISA 60th …, (1), pp. 1–5.
[21] Heath, S., 2000, "A New Technique For Identifying Synchronous Resonances Using Tip-Timing," Journal of Engineering for Gas Turbines and Power-Transactions of the ASME, 122(2), pp. 219–225.
[22] Russhard, P., 2010, "Development of a Blade Tip Timing Based Engine Health Monitoring System," Eng.D. dissertation, University of Manchester, Manchester, United Kingdom.
[23] Ma, H., Lu, Y., Wu, Z., Tai, X., Li, H., and Wen, B., 2015, "A New Dynamic Model of Rotor–blade Systems," Journal of Sound and Vibration, 357, pp. 168–194.